Journal of Power Sources 662 (2026) 238731

Contents lists available at ScienceDirect

Journal of Power Sources

journal homepage: www.elsevier.com/locate/jpowsour

Janus bilayer poly(vinyl alcohol)-based composite hydrogels with tunable photothermal and thermoelectric properties for photothermoelectric energy conversion

Yu-Hao Wang [a], Ching-Chieh Hsu [a], Shao-Huan Hong [a], Chih-Wei Hsu [a], Shiao-Wei Kuo [b], U-Ser Jeng [c], Shih-Huang Tung [d], Cheng-Liang Liu [a,d,e,*]

[a] Department of Materials Science and Engineering, National Taiwan University, Taipei, 10617, Taiwan
[b] Department of Materials and Optoelectronic Science, National Sun Yat-sen University, Kaohsiung, 80424, Taiwan
[c] National Synchrotron Radiation Research Center, Hsinchu, 30076, Taiwan
[d] Institute of Polymer Science and Engineering, National Taiwan University, Taipei, 10617, Taiwan
[e] Advanced Research Center for Green Materials Science and Technology, National Taiwan University, Taipei, 10617, Taiwan

HIGHLIGHTS

- Janus PVA hydrogels with CNT/rGO enable efficient photothermal conversion.
- Solvent ratio tuning optimizes Seebeck coefficient and thermal conductivity.
- Photothermoelectric generator shows stable voltage output under solar irradiation.

GRAPHICAL ABSTRACT

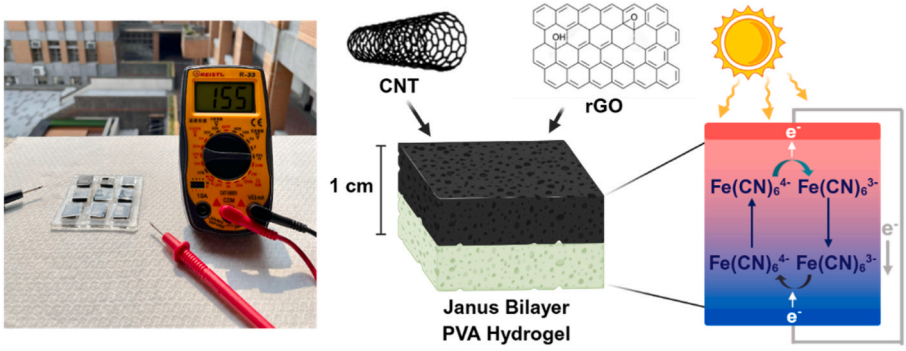

ARTICLE INFO

Keywords:
Hydrogel
Photothermoelectric
Poly(vinyl alcohol)
Thermoelectric
Photothermal
Carbon-based nanomaterials

ABSTRACT

Solar energy conversion through photothermoelectric (PTE) systems offers an efficient strategy for transforming solar heat into electricity. Herein, a Janus bilayer poly(vinyl alcohol) (PVA)-based PTE conversion hydrogel is successfully developed by incorporating carbon-based nanomaterials in the upper layer and systematically adjusting the dimethyl sulfoxide (DMSO):water (H_2O) solvent ratio to regulate the hydrogel's thermal and ionic transport properties. Specifically, the upper layer of the hydrogel is modified with carbon nanotubes (CNT) and reduced graphene oxide (rGO) to enhance the photothermal (PT) absorption, while the bottom pure PVA hydrogel maintains low thermal conductivity to preserve the temperature gradient. After immersion in a $K_4[Fe(CN)_6]/K_3[Fe(CN)_6]$ redox solution, the bilayer hydrogel achieves the low thermal conductivity of 0.42 W m^{-1} K^{-1} and high ionic Seebeck coefficient of 1.78 mV K^{-1} by adjusting the DMSO:H_2O ratio. Under simulated sunlight, the photothermoelectric generator (PTEG) exhibits the maximum temperature difference of 11.5 °C, voltage generation of 175 mV, and peak power density of 300 mW m^{-2}, with excellent outdoor stability. Unlike

* Corresponding author. Department of Materials Science and Engineering, National Taiwan University, Taipei 10617, Taiwan.
E-mail address: liucl@ntu.edu.tw (C.-L. Liu).

https://doi.org/10.1016/j.jpowsour.2025.238731
Received 24 August 2025; Received in revised form 19 October 2025; Accepted 30 October 2025
Available online 6 November 2025

conventional thermoelectric hydrogels, which primarily focus on single-layer structures or filler modulation, the Janus bilayer hydrogel offers notable advantages, including flexibility, low thermal conductivity, and ease of fabrication. These attributes highlight its potential for application in solar-powered devices.

1. Introduction

With the growing demand for sustainable and portable energy solutions, self-powered systems that are capable of harvesting ambient energy have become an increasingly important area of research [1,2]. As an abundant and renewable resource, solar energy plays a pivotal role in modern energy technologies [3]. Among the various forms of solar energy utilization, low-grade thermal energy remains a significant yet underutilized component of energy recovery strategies. In this context, photothermoelectric (PTE) conversion, which synergistically combines photothermal (PT) and thermoelectric (TE) effects to convert solar energy into electricity, has emerged as a promising pathway for next-generation energy-harvesting technologies [4–10]. This dual-mode energy conversion process involves the absorption of sunlight to generate heat, followed by TE conversion driven by the resulting temperature gradient [11]. Due to its inherent scalability and potential for off-grid applications, PTE conversion is well-suited for the development of next-generation energy-harvesting technologies.

Carbon-based nanomaterials such as carbon nanotubes (CNTs) and reduced graphene oxide (rGO) have been widely explored for PTE applications due to their strong near-infrared (NIR) absorption and high PT conversion efficiency [12–17]. When incorporated into PTE systems, these materials effectively enhance the solar-to-heat conversion. However, the existing PTE systems face several persistent challenges. First, while the PTE performance strongly depends on maintaining a stable temperature gradient, inefficient thermal management often results in rapid heat dissipation, thereby diminishing the temperature difference and limiting the TE output. Second, many existing PTE materials exhibit sensitivity to environmental conditions and limited long-term stability, which constrains their practical deployment in real-world applications. Consequently, improving the energy conversion efficiency and optimizing the integration of PT and TE components remain key challenges for advancing high-performance PTE devices.

To address these issues, several studies have explored integrated material strategies. For example, Shen et al. designed an interlocked PT layer hydrogel based on polyacrylamide (PAAM) and soaked in a pyrogallol and polyethyleneimine solution to achieve a Seebeck coefficient of -1.40 mV K^{-1} and a maximum power output of 1.47 mW m^{-2} under simulated sunlight (100 mW cm^{-2}). Although the surface temperature reached 63.4 °C, the resulting temperature difference was limited to 1.9 K [18]. Similarly, Bai et al. utilized an $Fe(CN)_6^{3-/4-}$ redox couple in polyvinyl alcohol (PVA) and gelatin-based hydrogel with a dimethyl sulfoxide (DMSO)/water (H_2O) binary solvent system to improve both the transparency and stretchability of the material. Further, they introduced a porous light-absorbing sponge as an external PT module to generate a maximum temperature difference of approximately 11.2 K, an open-circuit voltage of 16.6 mV, and a short-circuit current exceeding 100 μA after 12 h of illumination [19]. Despite these advances, many current PTE designs continue to face challenges such as insufficient temperature difference and excessively high thermal conductivity, as well as issues with interfacial adhesion and long-term stability.

Hence, the present study introduces a Janus bilayer hydrogel architecture that provides a more integrated materials strategy. Compared to single-layer homogeneous designs, the Janus bilayer configuration enables a directional control of heat flow and more effective coupling between PT conversion and TE response. In this architecture, the upper PT layer containing CNTs and rGO serves as a strong solar absorber, rapidly converting incident light into localized heat. The lower pure PVA layer, on the other hand, exhibits low thermal conductivity, which effectively suppresses downward heat dissipation and sustains a pronounced vertical temperature gradient across the interface. This anisotropic thermal distribution ensures that the heat flux is preferentially guided toward, thereby maintaining a stable driving force for redox potential difference formation. Such a design not only improves thermal management but also enhances the overall voltage output by stabilizing the temperature gradient over time. Furthermore, both layers share a chemically compatible PVA matrix, which eliminates interfacial delamination and ensures efficient PTE energy transfer. Consequently, the Janus bilayer structure plays a dual role: it maximizes solar absorption and heat generation in the upper layer while minimizing heat loss and preserving the temperature gradient through the lower layer. This synergistic mechanism is essential for achieving efficient and stable PTE conversion. Furthermore, this bilayer hydrogel is immersed in various volumes of $K_4[Fe(CN)_6]/K_3[Fe(CN)_6]$ redox solution in order to effect solvent exchange, thus leading to various DMSO:H_2O ratios. This strategy makes it possible to optimize the TE performance of the hydrogel, thereby achieves a high ionic Seebeck coefficient of 1.78 mV K^{-1} while maintaining a low thermal conductivity of 0.42 W m^{-1} K^{-1}. Under both simulated and natural sunlight, the resulting photothermoelectric generator (PTEG) delivers a maximum temperature difference of 11.5 °C, an output voltage of 175 mV, and a peak power density of 300 mW m^{-2}, which represents a significant advancement over previously reported hydrogel-based PTE systems (Table S1). Importantly, the device exhibits excellent long-term stability during outdoor operation. Overall, this work presents a simple, scalable, and flexible approach for integrating PT and TE functionalities within a unified hydrogel platform. Unlike previous PTE systems that suffered from poor interfacial coupling and unstable temperature gradients, the proposed Janus bilayer architecture achieves efficient PTE conversion through improved structural integration. The resulting PTEG holds considerable promise for applications in self-powered portable electronics and energy-harvesting devices, along with other next-generation energy systems.

2. Experimental section

2.1. Materials

Poly(vinyl alcohol) (PVA) with an average molecular weight (M_w) of 89,000–98,000 and a degree of hydrolysis of 99+%, potassium hexacyanidoferrate(II) ($K_4[Fe(CN)_6]\cdot 3H_2O$) (purity: 98.5%), and potassium ferricyanide ($K_3[Fe(CN)_6]$) (purity: 98%) were procured from Sigma-Aldrich. Single-walled carbon nanotubes (SWCNTs), with a diameter of less than 2 nm, a length greater than 5 μm, and 80 % purity), as well as were sourced from Tuball™. Graphene oxide (GO) powder (purity of 97% and thickness of 2–3 nm) were supplied from Taiwan Carbon Materials Corp. All chemicals were used as received without further purification. The synthesis details of reduced graphene oxide (rGO) are provided in the Supplementary Information, and the successful synthesis of rGO was confirmed through Fourier-transform infrared (FTIR) and X-ray diffraction (XRD) analyses, as depicted in Fig. S1.

2.2. Preparation of carbon-based dispersion

Aqueous dispersions of carbon-based nanomaterials (CNTs and/or rGO) were prepared for subsequent use in gel fabrication. For the individual dispersions, 5 or 10 mg of each carbon nanomaterial was combined with 2 mg of polyvinylpyrrolidone (PVP) and dispersed in 10 mL of deionized (DI) water. The mixtures were subjected to tip sonication for 2 h in an ice bath to ensure uniform dispersion. In addition, binary dispersions were formulated by mixing the carbon nanomaterials in the

following amounts: 10 mg CNTs + 10 mg rGO, 5 mg CNTs + 10 mg rGO, and 5 mg CNTs + 5 mg rGO. Each binary mixture was dispersed in 10 mL of DI water containing 2 mg of PVP, using the same sonication conditions. All dispersions were freshly prepared and used immediately for subsequent hydrogel synthesis.

2.3. Preparation and characterization of photothermoelectric hydrogel

The preparation process of the bilayer PTE hydrogel is illustrated in Fig. 1a. Here, PVA was selected as the hydrogel matrix due to its environmental friendliness, biodegradability, and low production cost. Also, it was expected to impart suitable flexibility and elasticity due to its mobile polymer chains within the hydrogel. The first (bottom) layer was prepared by dissolving 600 mg of PVA in 5 mL of dimethyl sulfoxide (DMSO) at 85 °C under continuous stirring until a clear solution was obtained. The resulting solution was cast into a polytetrafluoroethylene (PTFE) mold and subjected to a freeze–thaw cycle to induce gelation. The gel was retained in the mold for subsequent layer assembly. For the second (top) layer, 600 mg of PVA was dissolved in 4.5 mL of DMSO at 85 °C with stirring. After complete dissolution, 0.5 mL of the desired carbon-based dispersion was added to the solution and mixed thoroughly to form a homogeneous suspension. This mixture was carefully poured over the first-layer gel within the same PTFE mold and subjected to two additional freeze–thaw cycles to complete the bilayer gel formation. The PT hydrogels that were prepared using the single-component 5 mg CNT, 10 mg CNT, and 10 mg rGO dispersions are referred to hereafter as the **PT-5C**, **PT-10C**, and **PT-10R**, respectively. The hydrogels that were prepared using the binary dispersions (10 mg CNT + 10 mg rGO, 5 mg CNT + 10 mg rGO, and 5 mg CNT + 5 mg rGO) are designated as the **PT-10C10R**, **PT-5C10R**, and **PT-5C5R**, respectively.

To introduce the redox couple, aqueous solutions of 0.42 M $K_4[Fe(CN)_6]\cdot 3H_2O$ and 0.25 M $K_3[Fe(CN)_6]$ were prepared in DI water. Because the hydrogel undergoes solvent exchange when immersed in the redox solution, various volumes of the redox solution were used according to the volume of hydrogel. For this investigation, samples of the optimal bilayer hydrogel (**PT-5C10R**) were immersed in each redox solution, as depicted in Fig. 1. This solvent-exchange process enabled the formation of hydrogels with various DMSO: H_2O ratios (1:1, 1:2, 1:4, 1:8, and 1:10), thereby tuning the internal composition and charge transport properties. The resulting hydrogels are designated hereafter as the **PTE-1**, **PTE-2**, **PTE-4**, **PTE-8**, and **PTE-10**, respectively.

2.4. Fabrication of photothermoelectric generator

To fabricate the PTEG, a polydimethylsiloxane (PDMS) mold was first fabricated by mixing the base elastomer and curing agent in a 10:1 weight ratio, followed by curing at 80 °C. The final mold had dimensions of 6 × 6 × 1 cm^3, and contained nine internal cavities, each measuring 1 × 1 × 1 cm^3, into which individual PTE hydrogel blocks (1 × 1 × 1 cm^3 each) were inserted. Indium tin oxide (ITO) glass was employed as the electrode material and positioned on the top and bottom surfaces of the assembled hydrogel array. The use of ITO glass enabled optical transparency, thereby allowing sunlight to reach the hydrogels without compromising their PT performance. Copper wires were used to electrically connect the ITO electrodes in series across the nine hydrogel units. The entire PTEG was encapsulated using polyimide (PI) tape to ensure mechanical integrity and environmental stability during operation.

3. Results and discussion

3.1. Preparation of janus bilayer photothermoelectric hydrogel

The two-step fabrication procedure of the Janus bilayer PTE hydrogel is shown schematically in Fig. 1a and described in detail in the Experimental section. First, a bottom layer consisting of pristine PVA was prepared, and then a top layer containing the carbon-based PT nanomaterials was deposited onto the surface of the base layer. This top layer is responsible for absorbing solar radiation and generating a temperature gradient across the hydrogel. The two layers were then integrated via a freeze–thaw cycling process, which resulted in a physically crosslinked bilayer hydrogel, as confirmed by the morphological analysis below [20]. The as-prepared bilayer hydrogel was then immersed in the $K_4[Fe(CN)_6]/K_3[Fe(CN)_6]$ redox solution to enable ionic conduction and TE functionality. Additionally, solvent exchange was performed during the immersion process to achieve various DMSO: H_2O ratios within the hydrogel, with the aim of modulating the ionic transport properties of the matrix.

To endow the hydrogel with PT functionality, various carbon-based

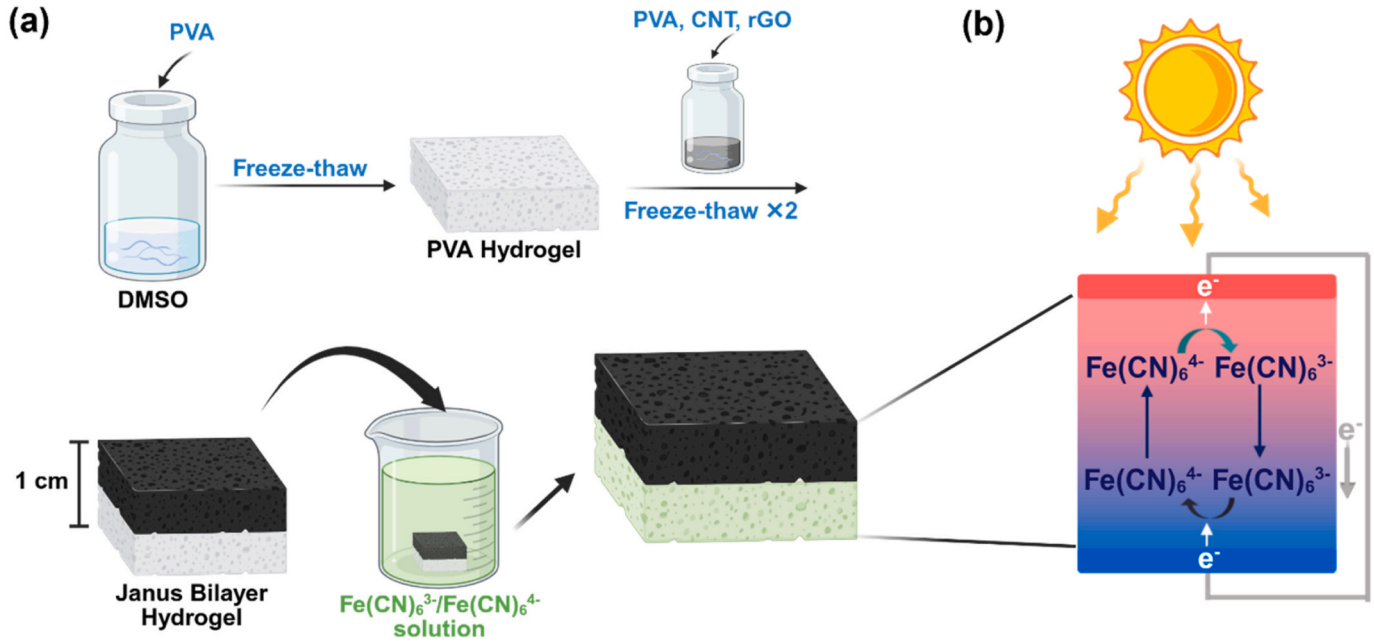

Fig. 1. Schematic illustration of janus bilayer hydrogel (a) preparation process and (b) the underlying PTE energy conversion mechanism.

nanomaterials, namely carbon nanotubes (CNT) and/or reduced graphene oxide (rGO), were incorporated into the upper layer. These materials were selected for their strong NIR light absorption capabilities and high PT conversion efficiency, which makes them beneficial for enhancing the PTE performance. The Janus bilayer configuration offers several strategic advantages. First, the monolithic integration of the two layers avoids interfacial mismatch, which can be expected to significantly improve the mechanical integrity and reduce the likelihood of delamination. This design also simplifies the fabrication process by eliminating the need for adhesives or additional assembly steps. Moreover, the vertical architecture is expected to facilitate the formation of a substantial temperature gradient across the hydrogel under solar irradiation, with the top layer acting as the photothermal "hot" side and the bottom layer as the relatively cooler side. In turn, this thermal gradient is expected to enhance the redox potential of the $Fe(CN)_6^{3-/4-}$ couple, thereby enabling efficient PTE voltage generation. To achieve redox-active functionality, the as-fabricated bilayer hydrogels were immersed in $Fe(CN)_6^{3-/4-}$ solution with various DMSO:H_2O volume ratios. As demonstrated in the following paragraphs, solvent exchange during this step enables the formation of hydrogels with tunable TE and ion transport properties. As shown in Fig. 1b, under solar irradiation, the bilayer hydrogel demonstrates effective PTE conversion, which is driven by the directional redox reaction between $Fe(CN)_6^{3-}$ and $Fe(CN)_6^{4-}$ across the thermal gradient.

3.2. Morphology and structural characterization of hydrogel containing carbon-based nanomaterials

Representative photographs of the various hydrogels are presented in Fig. S2, and their morphologies are revealed by the scanning electron microscopy (SEM) images in Fig. 2. Here, all samples exhibit a porous microstructure, thereby indicating that the inclusion of carbon nanomaterials does not compromise the integrity of the PVA hydrogel network [21,22]. Instead, their presence appears to promote or sustain the formation of a stable porous architecture. Such porosity is expected to be advantageous for PTE conversion, as it should not only enhance the mechanical flexibility and compliance of the material but also contribute to a reduction in the thermal conductivity, thereby facilitating the maintenance of a significant temperature gradient across the hydrogel (Table S2). Although CNT typically induce anisotropic heat conduction when aligned, the uniformly dispersed CNT and rGO within the hydrogel network do not form long-range oriented pathways. Consequently, the bilayer hydrogel exhibits no distinct in-plane/out-of-plane anisotropy, but instead maintains a stable vertical temperature gradient under irradiation [23]. This moderate thermal insulation plays a critical role in sustaining the thermoelectric driving force and achieving enhanced PTE performance.

The chemical structure and interactions between the PVA matrix and carbon-based additives are elucidated by the Fourier transform infrared (FTIR) spectra of the pristine PVA and the **PT-5C**, **PT-10C**, and **PT-10R** hydrogels in Fig. S3. Here, the broad peak centered at around 3410 cm^{-1} corresponds to the stretching vibrations of hydroxyl (–OH) groups in PVA, thereby indicating the presence of hydrogen bonding within each hydrogel network (Fig. S3a). Meanwhile, the absorption band near 1640 cm^{-1} is attributed to O–H bending vibrations in PVA. The band at 1440 cm^{-1} arises from the bending vibrations of the methylene ($–CH_2$) groups, while the signal at around 1320 cm^{-1} is associated with the bending vibrations of C–H groups or the sulfoxide (S=O) bending of

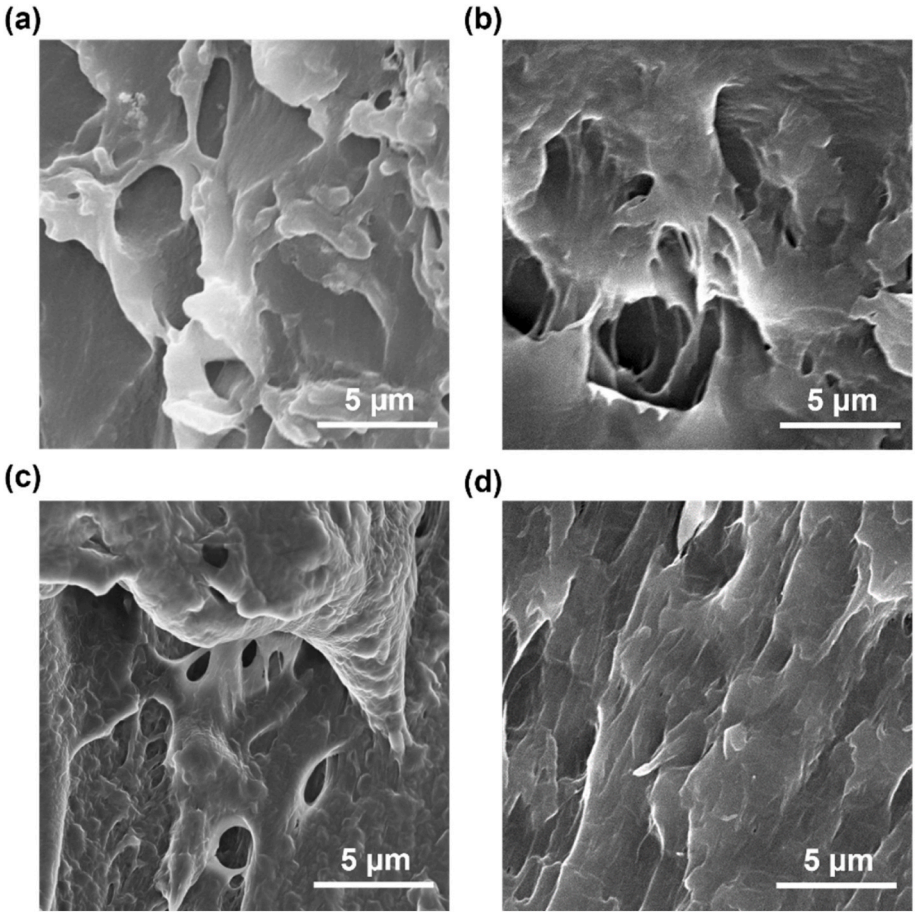

Fig. 2. Morphological characterization of hydrogels incorporating carbon-based nanomaterials. SEM images at a magnification of 5000 × magnification of (a) pure PVA, (b) **PT-10C**, (c) **PT-10R** and (d) **PT-5C10R** hydrogels.

DMSO. Additionally, a distinct peak at 1020 cm^{-1} is associated with the C–O stretching vibrations, which relate to the PVA matrix and may overlap with the symmetric S=O stretching from DMSO [24,25]. Importantly, no significant peak shifts or new functional group absorptions are observed in the spectra of the nanomaterial-loaded hydrogels, thereby indicating that the addition of carbon-based nanomaterials does not induce any chemical modifications to the PVA backbone. This suggests that the nanomaterials are well dispersed within the hydrogel matrix in a physically embedded state, without altering the intrinsic chemical structure of the host polymer network. The retention of these characteristic spectral features confirms the integrity of the PVA matrix across all composite formulations.

3.3. *Photothermal properties of hydrogel incorporating carbon-based nanomaterials*

The PT behavior of the composite hydrogels under AM1.5G solar irradiation is revealed by the infrared thermal images in Fig. 3a–c, while the time-dependent changes in temperature at both the hot (T_H) and cold (T_C) ends are shown in Fig. 3d–f and S4–S5. Here, the **PT-10C** hydrogel exhibits a maximum surface temperature of 48.7 °C on the irradiated (hot) side, while the **PT-10R** hydrogel reaches only 40.0 °C (Fig. 3a and d, and Fig. S4a and S5a). Thus, the **PT-10C** demonstrates an enhanced PT performance relative to **PT-10R**. Meanwhile, the **PT-5C** hydrogel exhibits a maximum surface temperature of 49.7 °C (Figs. S4b and S5b), which is higher than both the **PT-10C** and the **PT-10R**. This indicates that the **PT-10C** exhibits the best PT performance among the three investigated hydrogels. Among the various binary hydrogels, the **PT-5C10R** exhibits the highest surface temperature of 52.5 °C (Fig. 3c and f), compared to 48.0 °C for the **PT-5C5R** hydrogel (Figs. S4c and S5c), and 49.0 °C for the **PT-10C10R** hydrogel (Fig. 3b and e). Moreover, the **PT-5C10R** hydrogel exhibits a maximum temperature gradient of approximately 12.0 °C between the hot and cold ends (Table S1). When a single PT material is incorporated into the hydrogel, higher concentrations can achieve higher temperatures. However, when two PT materials are introduced simultaneously, a proper ratio can generate a synergistic effect that enhances light harvesting and heat conversion, thereby achieving higher temperatures. Conversely, excessively high concentrations lead to optical shielding, which reduces absorption efficiency and prevents further temperature increase. The ratios in **PT-10C10R** and **PT-5C10R** are close to the optimal range, allowing them to reach higher temperatures. This phenomenon is closely related to the optimization of PT material concentration. Thus, among the tested formulations, the **PT-5C10R** hydrogel demonstrates the most effective PT conversion performance.

The superior performance of the **PT-5C10R** hydrogel can be attributed to the optimized combination of strong NIR absorption and efficient thermal conduction from the rGO and CNT components [13,26]. Conversely, due to their high thermal conductivity, an excessive loading of CNTs can promote rapid heat dissipation and reduce the overall temperature gradient. Therefore, the present results suggest that the CNT content must be limited to 0.5 mg mL^{-1} in order to mitigate this effect and maintain optimal thermal management. Meanwhile, the highly porous morphology of the PT hydrogels (Fig. 2) enhances the

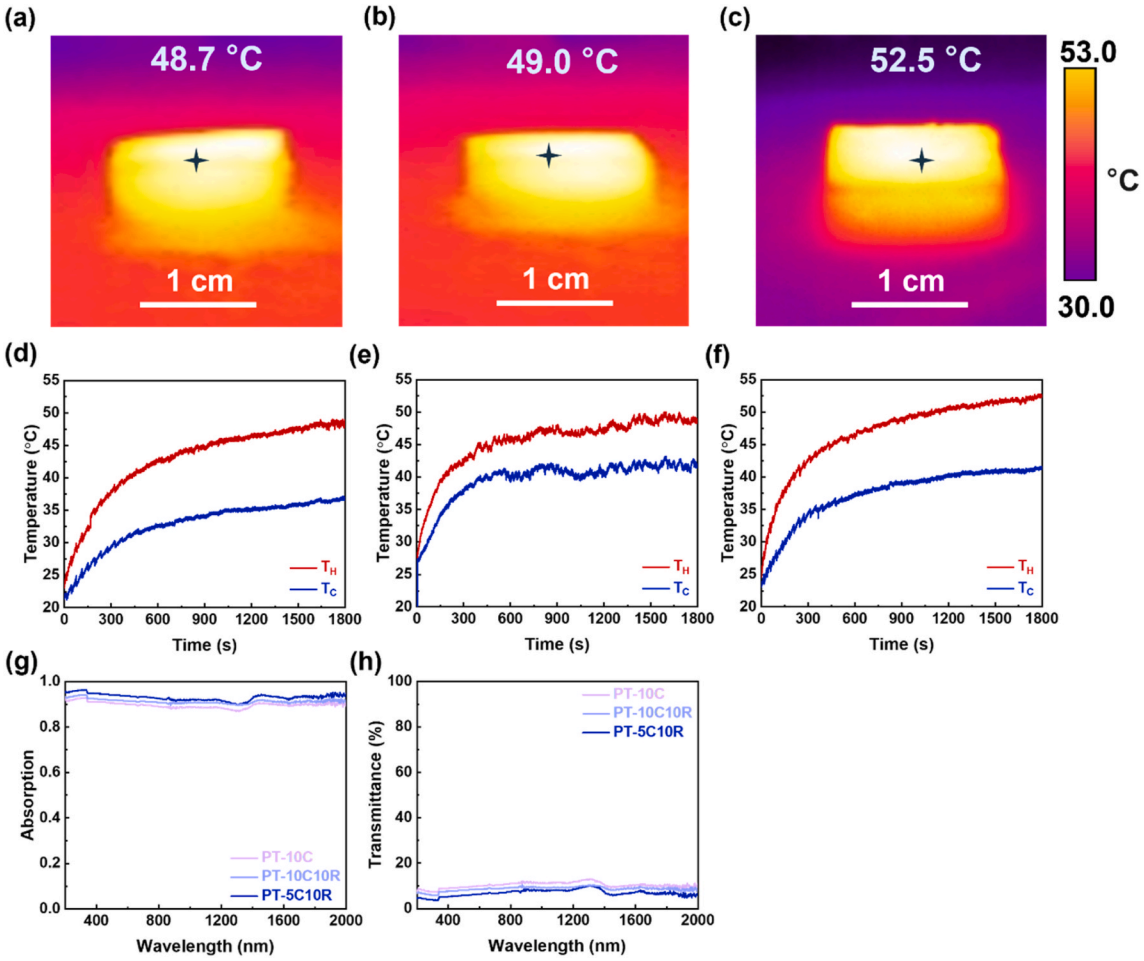

Fig. 3. PT properties of hydrogels under solar irradiation. Infrared thermal images showing the surface temperature of (a) **PT-10C**, (b) **PT-10C10R**, and (c) **PT-5C10R** hydrogels. Temperature profiles of the hot and cold sides over time for (d) **PT-10C**, (e) **PT-10C10R**, and (f) **PT-5C10R** hydrogels. UV–vis–NIR spectra showing (g) normalized absorbance curves and (h) transmittance curves of the hydrogels.

light trapping and surface absorption via multiple scattering effect, thereby further improving the localized heating effect [21,22]. Furthermore, the above FTIR analysis confirms that the addition of CNTs and rGO does not significantly alter the chemical structure of the PVA hydrogel, thereby indicating physical dispersion of the carbon-based nanomaterials within the polymer matrix.

Preservation of the gel's inherently low thermal conductivity is critical for maintaining a substantial temperature gradient during operation. Hence, the PT responses of the **PT-10C**, **PT-10C10R**, and **PT-5C10R** hydrogels are further elucidated by the corresponding UV–vis–NIR optical absorption and transmittance spectra in Fig. 3g and h, respectively. Thus, each hydrogel exhibits strong broadband absorption, reaching approximately 90% across the entire measured spectrum (Fig. 3g), along with minimal light transmission (Fig. 3h and S6d), thereby further validating the strong light-harvesting capability of the CNTs and rGO [27,28]. Moreover, the additional spectral measurements in Fig. S6a and S6c reveal that the **PT-10R** hydrogel exhibits comparatively weaker light absorption compared to the **PT-10C**, which is consistent with the visibly lighter appearance of the former sample (Fig. S2, Fig. S6a and c). Similarly, the **PT-5C** hydrogel displays a slightly reduced light absorption capability compared to the **PT-10C** (Fig. S6b and S6d). This can be attributed to the lower concentration of PT fillers, which limits their solar energy harvesting efficiency. However, it is important to note that strong absorbance in the UV–vis spectra does not always correlate with a higher temperature gradient, as additional factors such as light scattering and thermal dissipation may each play a role.

In view of the above results, a CNT concentration of 0.5 mg mL^{-1} was selected as the optimal loading, and its effects on both the temperature increase and temperature gradient were examined in the binary CNT/rGO dispersions. In this case, as shown in Figs. S4 and S5, although the **PT-5C5R** exhibit an improved PT performance relative to the **PT-5C**, it is outperformed by the **PT-5C10R**, thereby highlighting the benefit of an increased rGO content at a fixed CNT level. Conversely, although the **PT-10C10R** exhibits strong light absorption, its PT performance is slightly poorer than that of **PT-5C10R**, as shown in Fig. 3e and f. This can be attributed to an excessive concentration of total carbon-based nanomaterials, which can cause excessive light reflection, internal shielding, and reduced penetration of solar radiation into the hydrogel, thereby reducing the net effective absorption and temperature conversion [29,30]. Thus, an optimized composition of 5 mg CNTs and 10 mg rGO is found to provide a suitably balanced and synergistic PT network. These results collectively indicate the importance of carefully tuning both the compositional ratio and absolute amounts (concentrations) of carbon-based nanomaterials to achieve optimal solar energy harvesting and PT conversion efficiency. In particular, the optimized **PT-5C10R** hydrogel demonstrates excellent potential for PTE applications, where efficient thermal energy conversion and precise temperature management are critical.

3.4. Thermoelectric properties of hydrogels with varying DMSO:H_2O ratios

As detailed in the Experimental section, the optimal **PT-5C10R** hydrogel was subsequently immersed in various volumes of $K_4[Fe(CN)_6]/K_3[Fe(CN)_6]$ to yield the **PTE-1**, **PTE-2**, **PTE-4**, **PTE-8**, and **PTE-10** samples shown in Fig. S7. The TE performance was then evaluated according to the ionic Seebeck coefficient (S_i), which quantifies the voltage generated per unit temperature difference. Mathematically, this parameter is defined as $S_i = -\Delta V/\Delta T$, where ΔV is the generated thermovoltage and ΔT is the applied temperature gradient [31–39]. The measured TE responses of the various samples under ambient conditions (relative humidity = 50–70%) are shown in Fig. 4a. This response arises from the temperature-dependent redox reactions of the $Fe(CN)_6^{3-/4-}$ couple, including oxidation ($Fe(CN)_6^{4-} \rightarrow Fe(CN)_6^{3-} + e^-$) at the hot end and reduction ($Fe(CN)_6^{3-} + e^- \rightarrow Fe(CN)_6^{4-}$) at the cold end [40–46]. This thermodynamically asymmetric redox behavior drives electron flow from the cold end to the hot end, thereby generating a measurable voltage output for the thermogalvanic cell. As shown in Fig. 4a, the relationship between ΔV and ΔT is linear for all compositions, from which the S_i values are extracted via the slopes of the fitted lines. Thus, the calculated S_i values are 0.69, 0.77, 1.29, 1.78, and 1.54 mV K^{-1} for

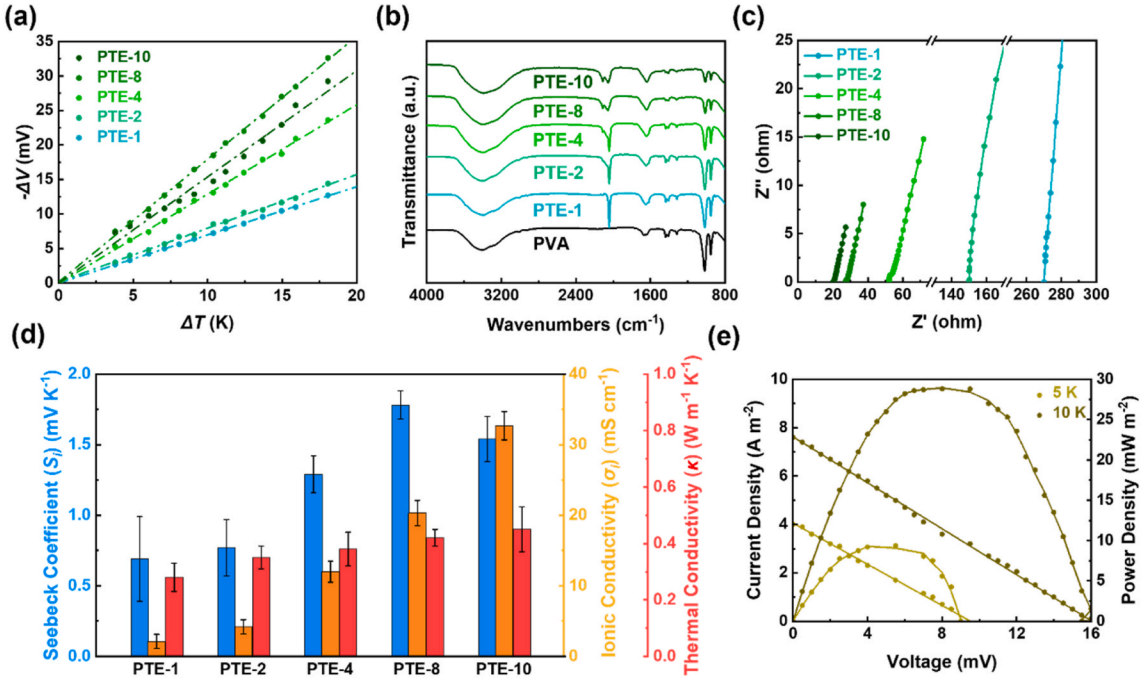

Fig. 4. TE properties and structural characterization of hydrogels with varying DMSO:H_2O ratios. (a) $-\Delta V$–ΔT curves, where the slope corresponds to the ionic Seebeck coefficient. (b) FTIR spectra of the hydrogels. (c) Electrochemical impedance spectroscopy spectra, with the intercept used to calculate ionic conductivity. (d) Comparison of ionic Seebeck coefficient, ionic conductivity, and thermal conductivity among different hydrogel formulations. (e) Current density–voltage and power density–voltage characteristics of the **PTE-8** hydrogel.

the **PTE-1**, **PTE-2**, **PTE-4**, **PTE-8**, and **PTE-10**, respectively. These results indicate that the **PTE-8** exhibits the highest S_i, thereby providing the most favorable TE performance.

The above trend is further supported by the FTIR analysis of the various PTE hydrogels in Fig. 4b. Here, characteristic absorption peaks corresponding to the C≡N stretching vibrations of the $Fe(CN)_6^{3-/4-}$ redox couple can be observed in the 2100–2150 cm^{-1} region. Specifically, the **PTE-1**, **PTE-2**, and **PTE-4** hydrogels each exhibit a single absorption band, thereby suggesting minimal electrochemical potential difference between the oxidized and reduced redox species. This is likely due to the relatively high DMSO content, which provides a more uniform and less perturbing solvation environment for the redox couple. By contrast, distinct dual peaks are observed for the **PTE-8** and **PTE-10** hydrogels, thereby indicating a more pronounced differentiation in redox state environments as the water content is increased [47,48]. This suggests that the differing polarities and hydrogen-bonding capabilities of water and DMSO modify the solvation shells and ion-solvent interactions of the redox couple, thereby enhancing the Gibbs free energy difference and thermovoltage output under a thermal gradient. Overall, these results confirm that the **PTE-8** hydrogel provides the optimal solvation environment for maximizing the redox separation and S_i value [49].

The ionic conductivity (σ_i) of each sample can be obtained by using the equation $\sigma_i = d/(A \times R)$, where d is the sample thickness, A is the cross-sectional area, and R is the bulk resistance obtained from the electrochemical impedance spectroscopy (EIS) Nyquist plots in Fig. 4c [50–56]. Thus, the σ_i values of the **PTE-1**, **PTE-2**, **PTE-4**, **PTE-8**, and **PTE-10** samples were measured as 2.1, 4.2, 12.0, 20.3, and 32.7 mS cm^{-1}, respectively. This increasing trend reflects the improved solubility and mobility of the $Fe(CN)_6^{3-/4-}$ redox couple in the systems with higher water content. As a highly polar solvent, water enhances ion dissociation and reduces ion aggregation, thereby promoting ionic conductivity [57,58]. Consequently, hydrogels with a higher water content, particularly the **PTE-8** and **PTE-10**, exhibit superior ionic conductivity.

As shown in Fig. 4d, the thermal conductivity (κ) is also found to increase with water content, giving values of 0.28, 0.35, 0.38, 0.42, and 0.45 W m^{-1} K^{-1} for the **PTE-1**, **PTE-2**, **PTE-4**, **PTE-8**, and **PTE-10**, respectively. This trend is attributed to the higher intrinsic thermal conductivity of water (~0.6 W m^{-1} K^{-1}) compared to DMSO (~0.2 W m^{-1} K^{-1}), which makes the water-dominant formulations more effective for heat conduction [59,60]. Among the various samples, the **PTE-8** emerges as the optimal formulation, offering the highest S_i of 1.78 mV K^{-1} along with a high σ_i of 20.3 mS cm^{-1}, while maintaining a relatively low κ of 0.42 W m^{-1} K^{-1}. This favorable balance ensures that a strong temperature gradient is preserved while enabling efficient ionic transport, both of which are critical for effective TE conversion.

The power-generating capability of a single **PTE-8** hydrogel is revealed by the measured current density–power density–voltage characteristics under thermal gradients of 5 K and 10 K in Fig. 4e. Thus, under a temperature difference of 5 K, the device produces an open-circuit voltage of 9 mV, a current density of ~4 A m^{-2}, and a maximum power density of 9.35 mW m^{-2}. When the temperature difference is increased to 10 K, however, the open-circuit voltage increases to 16 mV, the current density reaches ~7.6 A m^{-2}, and the maximum power density increases substantially to 28.8 mW m^{-2}. These results demonstrate a strong linear dependence of output power on the applied temperature difference, which is consistent with the measured ionic Seebeck coefficient and confirms the hydrogel's effectiveness for low-grade thermal energy harvesting.

3.5. Structures and mechanical properties of hydrogel with varying DMSO:H_2O ratios

The structural origins of mechanical behavior in the hydrogels with various DMSO:H_2O ratios are elucidated by the following small-angle X-ray scattering (SAXS), tensile testing, rheology, and SEM results. SAXS was employed to probe the internal microstructure of the hydrogels that cannot be fully resolved by SEM, tensile, or rheological measurements. This technique provides quantitative insights into the size, shape, and arrangement of polymer aggregates, thereby bridging the microscopic network characteristics with macroscopic mechanical and thermal behaviors. Here, the SAXS data were analyzed using the Beaucage two-level model, which effectively captures hierarchical structural features in polymeric networks. The scattering intensity $I(q)$ is modeled as:

$$I(q) \cong I_{bkg} + \sum_{i=1}^{N} \left\{ G_i \exp\left(-\frac{q^2 R_{gi}^2}{3} \right) + B_i \exp\left(-\frac{q^2 R_{g(i+1)}^2}{3} \right) \times \left\{ \frac{\left[erf\left(\frac{qR_{gi}}{\sqrt{6}} \right) \right]^3}{q} \right\}^{P_i} \right\}$$

where G_i is the Guinier pre-exponential factor, B_i is the power law pre-exponential factor, R_{gi} is the radius of gyration, P_i is the fractal dimension, and $i = 1$ corresponds to the global structure, while $i = 2$ relates to local structures. As shown in Fig. 5a, Fig. S8, and Table S3, the fitted P_1 value is around 2.8 for all hydrogel compositions, thereby suggesting a mass fractal structure consisting of a loosely packed, branched network of aggregated polymer chains. Meanwhile, the P_2 values range from 3 to 4 (Fig. 5a and S8, Table S3), which is characteristic of a surface fractal structure, thereby implying that the surfaces of the aggregated domains are rough and irregular. These results suggest that the hydrogels are maintained by fractal-like flocs of aggregated PVA particles with rough surfaces, regardless of the DMSO:H_2O ratio. Moreover, R_{g1} value also increases with the increase in water content, thereby indicating that the size of the aggregates becomes larger, which is consistent with the observed trend in tensile behavior. Meanwhile, the size of the individual PVA particles (R_{g2}) is consistently around 30 Å, within a minor margin of error [32,61–64].

The mechanical stress-strain measurements in Fig. 5b indicate clear compositional trends, such that the maximum stress of the hydrogel increases, and the strain at breaking point decreases, as the DMSO:H_2O ratio is decreased from 1:1 to 1:10. This suggests that the hydrogel network becomes stiffer but less stretchable with decreasing DMSO content (increasing water content). This mechanical evolution is primarily attributed to changes in polymer solubility and network crystallinity, which are governed by the solvent composition. Specifically, PVA exhibits a higher solubility in DMSO than in water. During freeze-thaw induced gelation, this solubility difference significantly influences microstructure formation. The hydrogels formed in water-rich solutions appear opaque, thereby indicating the aggregation tendency of PVA chains in water and the strong compressive forces exerted by ice crystallization [65,66]. These factors promote the development of extensive and unevenly distributed microcrystalline domains, which serve as rigid physical crosslinking points, as evidenced by the increase in R_{g1} with water content. As a result, the water-rich hydrogels exhibit higher stiffness and tensile strength but lower toughness due to localized stress concentration and limited polymer chain mobility. By contrast, the hydrogels derived from DMSO-rich solutions display greater transparency, which is indicative of a more homogeneous microstructure and reduced crystallinity. The enhanced dispersion of PVA chains in DMSO minimizes aggregation and allows for more uniform network formation. This leads to improved chain mobility and uniform stress distribution during deformation, thus yielding hydrogels with superior toughness and higher elongation at breaking point. Therefore, the solvent composition not only governs the polymer solubility and crystallization behavior, but also critically determines the mechanical performance and visual transparency [67,68].

These observations are further supported by the SEM images in Fig. S9. Here, the average pore size of the hydrogel is seen to decrease as

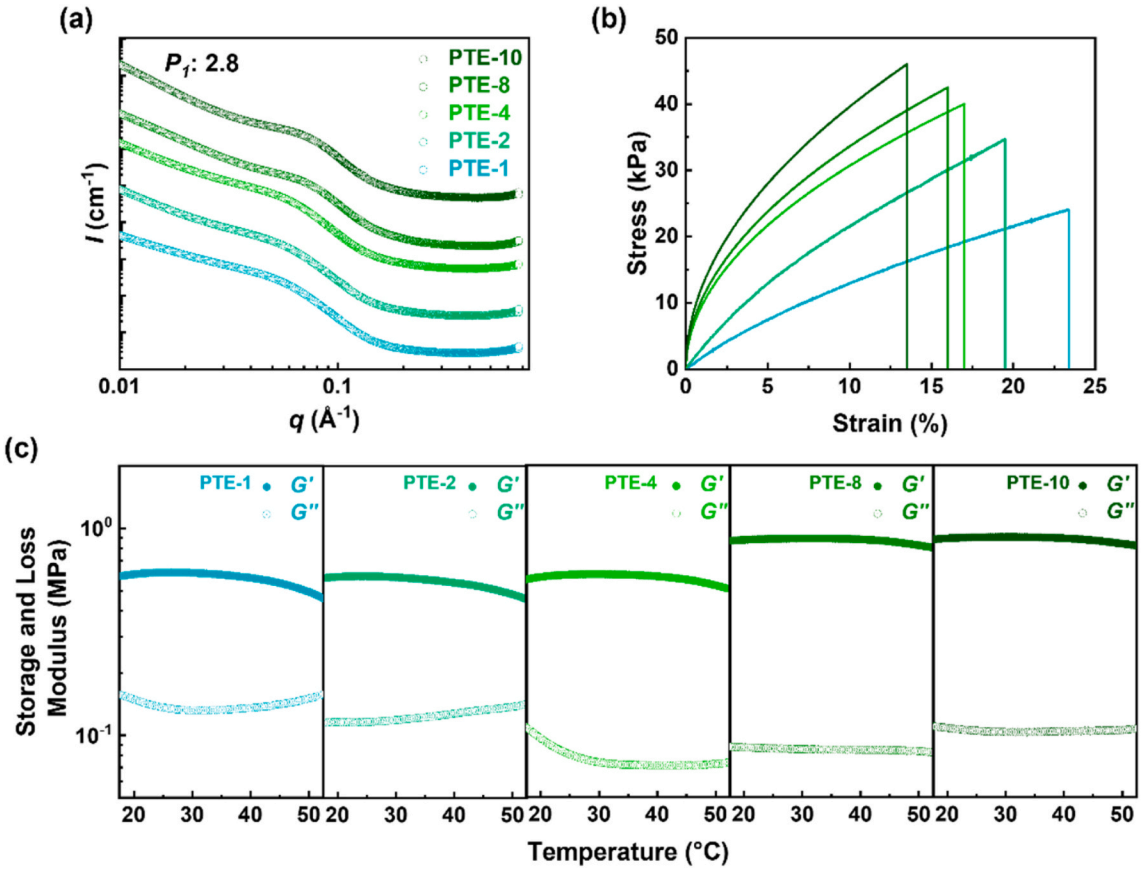

Fig. 5. Structural and mechanical characterization of PTE hydrogels with varying DMSO:H_2O ratios: (a) SAXS spectra, (b) tensile stress–strain curves, and (c) dynamic mechanical analysis showing storage modulus (G') and loss modulus (G'').

the water content increases, thereby indicating the formation of a denser and more compact network. The reduced porosity is consistent with the enhanced tensile strength and diminished elongation observed in the mechanical test results. This densification reflects the influence of water in promoting intermolecular interactions and tighter packing of the PVA chains. Furthermore, the rheological measurements in Fig. 5c indicate that the storage modulus (G') consistently exceeds the loss modulus (G'') for all of the hydrogels, thereby confirming dominant elastic (solid-like) behavior across the tested temperatures. Condition $G' > G''$ signifies that energy is primarily stored rather than dissipated during deformation, and is indicative of a well-established physically crosslinked gel network [69,70]. Notably, the **PTE-10** exhibits the highest G' value, which

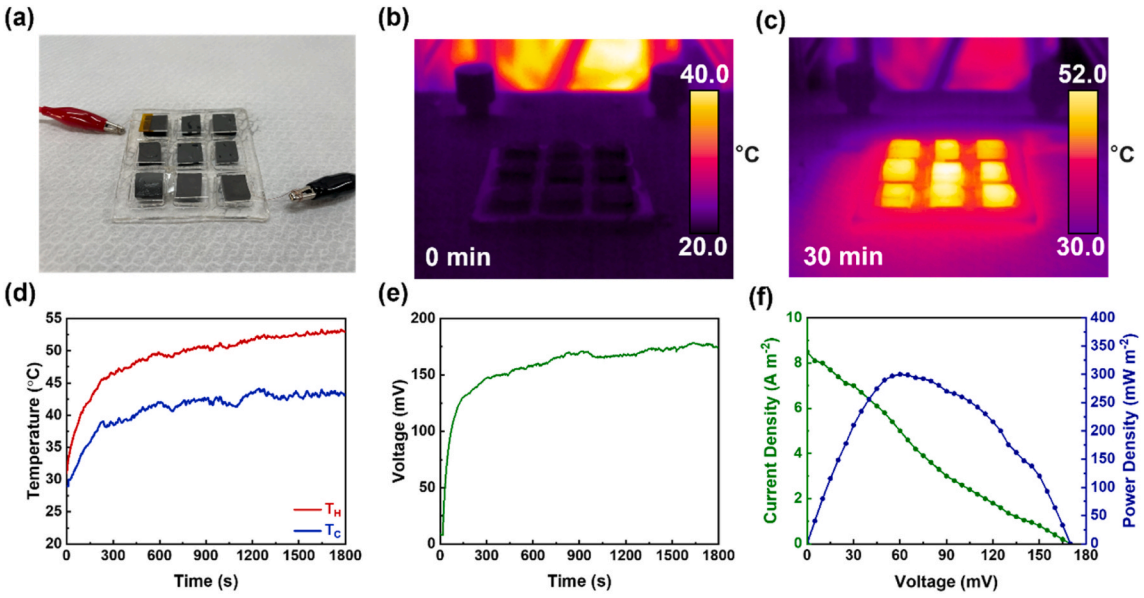

Fig. 6. (a) Photograph of the PTEG. Infrared thermal images of the PTEG under solar irradiation at (b) 0 min and (c) 30 min. (d) Temperature profiles of the hot and cold sides over time. (e) Voltage output as a function of time, and (f) current density–voltage and power density–voltage characteristics of the PTEG.

suggests strong elastic energy storage and minimal energy dissipation. As the water content is increased, the G' increases while G'' decreases, thereby indicating a transition toward more elastic and less dissipative network structures. Collectively, these results demonstrate that the mechanical and rheological properties of PVA-based hydrogels can be systematically tuned via solvent composition. By adjusting the DMSO: H_2O ratio, the network crystallinity and elasticity can be precisely modulated to achieve hydrogels ranging from soft and compliant to stiff and mechanically robust. This tunability is particularly advantageous for optimizing the shape stability and operational reliability in TE applications.

3.6. Photothermoelectric generator

To evaluate the integration of PT and TE functionalities, a PTEG was assembled by serially connecting nine **PTE-8** hydrogel units (1 × 1 × 1 cm^3 each) within a PDMS mold for mechanical support, as shown in Fig. 6a. Indium tin oxide (ITO)-coated glass was employed as both the top and bottom electrodes due to its favorable combination of high electrical conductivity and optical transparency. This configuration not only ensures efficient charge transport but also allows sunlight to penetrate the device, thereby facilitating effective PT activation and the generation of a vertical temperature gradient across the hydrogel units. Under AM1.5G simulated solar irradiation for 30 min, the thermal images in Fig. 6b and c reveal a steady increase in surface temperature from ambient conditions to approximately 52.0 °C, thereby demonstrating the efficient PT conversion capability of the system. Meanwhile, the temperatures at the hot and cold sides of the PTEG were also measured as a function of time, as shown in Fig. 6d, which shows a temperature difference of ~11.5 °C. Concurrently, the output voltage gradually increases and reaches a maximum of ~175 mV at the end of the illumination period (Fig. 6e). Furthermore, the PTE output of the device is evaluated by the current density–power density–voltage measurements under a temperature difference of ~11.5 °C in Fig. 6f. Here, the device exhibits an open-circuit voltage of ~175 mV, a current density of ~8.5 A m^{-2}, and a peak power density of ~300 mW m^{-2}. These values confirm that the Janus bilayer hydrogel system can effectively harvest both solar and thermal energy, thereby demonstrating strong potential for application in self-powered, sunlight-driven electronic devices.

Finally, the real-world applicability of the PTEG is evaluated by the results of outdoor performance testing, which was conducted under natural sunlight on the atrium of the College of Engineering, National Taiwan University, Taipei, in May 2025. As shown in Fig. 7a, the surface temperature and output voltage were continuously monitored between 10:00 and 20:00, and the surface temperature reached a maximum of 45.1 °C at 14:00. At this time, the corresponding open-circuit voltage reached 155 mV (Fig. 7b). Over the full 10 h period, the voltage output exhibits a positive correlation with the temperature change (Fig. 7c), thereby indicating reliable and continuous energy harvesting under varying environmental conditions. Furthermore, the results of repeatability and durability tests performed at 14:00 during seven consecutive days clearly indicate that, after solar exposure, the PTEG reliably generates an average open-circuit voltage of ~150 mV (Fig. 7d). Moreover, as shown in Table S1, the device fabricated herein generates a larger

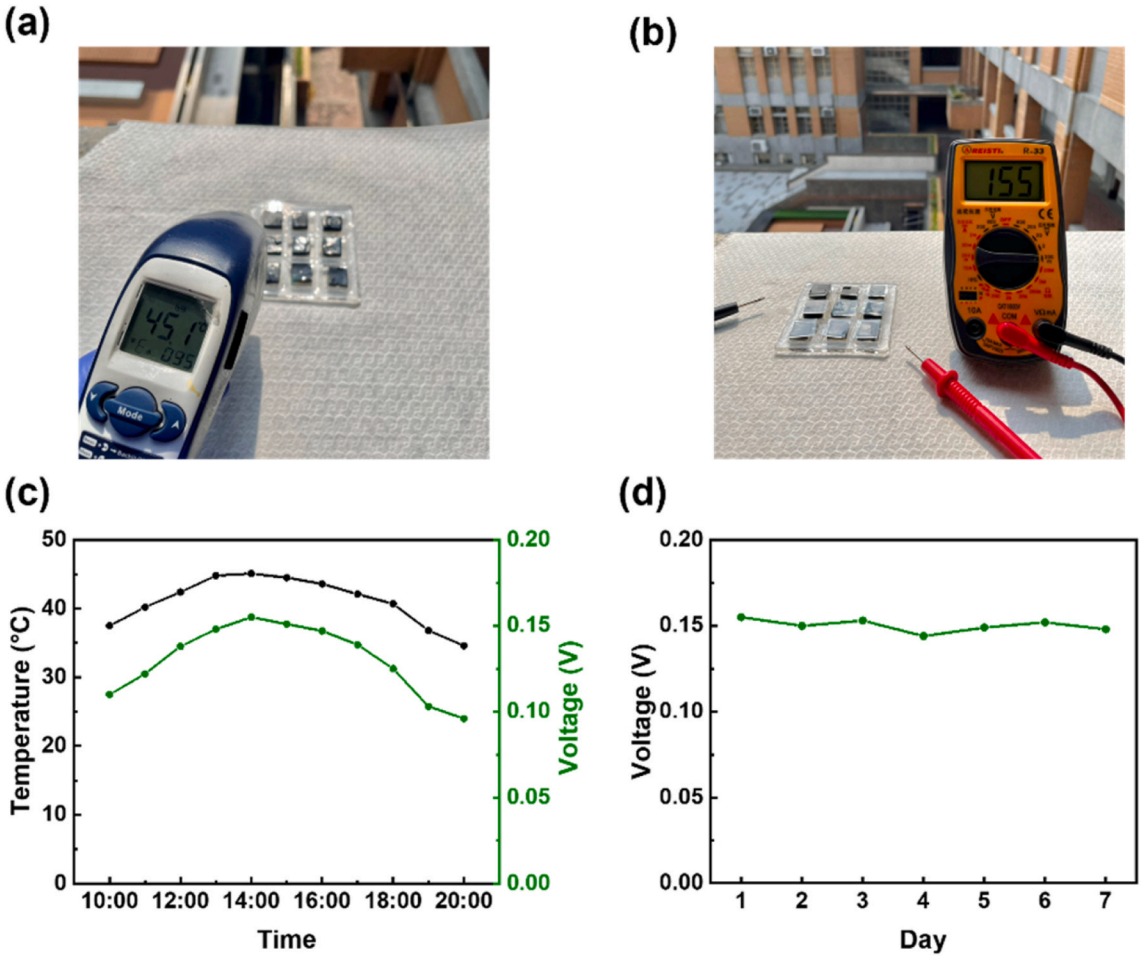

Fig. 7. Outdoor performance evaluation of the PTEG. (a) Temperature profile and (b) photographic image of the PTEG during outdoor testing. (c) Hot-side temperature and corresponding voltage output over a continuous 10 h period. (d) Voltage output measured at 14:00 across seven consecutive days.

temperature difference compared to previously reported hydrogel-based PTE systems, and also yields greater voltage and power outputs than previous PTEGs. These results demonstrate the device's robust operational stability, repeatable output behavior, and strong potential for long-term deployment in sustainable outdoor energy harvesting applications.

4. Conclusion

Herein, a poly(vinyl alcohol) (PVA)-based Janus bilayer hydrogel was successfully developed for efficient photothermoelectric (PTE) energy conversion. The upper layer, incorporating carbon nanotubes (CNTs) and/or reduced graphene oxide (rGO), enabled excellent photothermal (PT) conversion, while the lower layer, consisting of pure PVA hydrogel, served to maintain a low thermal conductivity and enhance the temperature gradient across the device. The Janus bilayer hydrogel was further functionalized through immersion in a $K_4[Fe(CN)_6]/K_3[Fe(CN)_6]$ redox solution to further enhance the temperature gradient across the device while optimizing the ionic Seebeck coefficient (1.78 mV K^{-1}) via precise tuning of the DMSO:H_2O ratio and maintaining a low thermal conductivity of 0.42 W m^{-1} K^{-1}. Consequently, the assembled photothermoelectric generator (PTEG) demonstrated a stable temperature increase and voltage output under both simulated and natural solar irradiation. Under AM1.5G solar conditions, the device achieved a maximum temperature difference of 11.5 °C, an open-circuit voltage of 175 mV, and a peak power density of 300 mW m^{-2}. Moreover, the PTEG exhibited excellent long-term operational stability during continuous outdoor testing. Overall, these findings validate the effectiveness of the Janus bilayer hydrogel design in achieving synergistic PT and thermoelectric functionalities. The demonstrated performance establishes this platform as a promising candidate for solar-powered, self-sustaining technologies, with potential applications in portable electronics, environmental monitoring, and next-generation energy-harvesting systems.

CRediT authorship contribution statement

Yu-Hao Wang: Writing – review & editing, Writing – original draft, Validation, Investigation, Formal analysis, Data curation, Conceptualization. **Ching-Chieh Hsu:** Data curation, Conceptualization. **Shao-Huan Hong:** Data curation, Conceptualization. **Chih-Wei Hsu:** Formal analysis, Data curation. **Shiao-Wei Kuo:** Data curation. **U-Ser Jeng:** Resources. **Shih-Huang Tung:** Formal analysis, Data curation. **Cheng-Liang Liu:** Writing – review & editing, Supervision, Funding acquisition, Conceptualization.

Declaration of competing interest

The authors declare that they have no known competing financial interests or personal relationships that could have appeared to influence the work reported in this paper.

Acknowledgements

The authors acknowledge financial support from the 2030 Cross-Generation Young Scholars Program by the National Science and Technology Council (NSTC) in Taiwan under grants 113-2628-E-002-028, the Academic Research-Career Development Project (Sprout Research Projects) from National Taiwan University (NTU114L7817), and the Advanced Research Center for Green Materials Science and Technology from the Featured Area Research Center Program as part of the Higher Education Sprout Project funded by the Ministry of Education in Taiwan (114L9006). The authors thank Beamline TPS 13A at the National Synchrotron Radiation Research Center (NSRRC) of Taiwan for providing beamtime. The authors gratefully thank Ms. Ya-Yun Yang for the assistance in SEM experiments of the Instrumentation Center at National Taiwan University, supported by the NSTC.

Appendix B. Supplementary data

Supplementary data to this article can be found online at https://doi.org/10.1016/j.jpowsour.2025.238731.

Data availability

Data will be made available on request.

References

[1] C. Jiang, X. Li, S.W.M. Lian, Y. Ying, J.S. Ho, J. Ping, Wireless technologies for energy harvesting and transmission for ambient self-powered systems, ACS Nano 15 (2021) 9328. https://doi.org/10.1021/acsnano.1c02819.
[2] M. Gholikhani, H. Roshani, S. Dessouky, A. Papagiannakis, A critical review of roadway energy harvesting technologies, Appl. Energy 261 (2020) 114388. https://doi.org/10.1016/j.apenergy.2019.114388.
[3] A.O. Maka, J.M. Alabid, Solar energy technology and its roles in sustainable development, Clean Energy 6 (2022) 476. https://doi.org/10.1093/ce/zkac023.
[4] C.-H. Yin, H.-T. Jiang, L.-D. Chen, Y.-Y. Lv, S.-H. Yao, J. Zhou, Y. Chen, M.-H. Lu, Y.-F. Chen, Key parameters to optimize the photothermoelectric effect of thermoelectric materials, J. Appl. Phys. 136 (2024) 073103. https://doi.org/10.1063/5.0219048.
[5] S. Hong, G. Zou, H. Kim, D. Huang, P. Wang, H.N. Alshareef, Photothermoelectric response of $Ti_3C_2T_x$ MXene confined ion channels, ACS Nano 14 (2020) 9042. https://doi.org/10.1021/acsnano.0c04099.
[6] X. Lu, L. Sun, P. Jiang, X. Bao, Progress of photodetectors based on the photothermoelectric effect, Adv. Mater. 31 (2019) 1902044. https://doi.org/10.1002/adma.201902044.
[7] M. Dai, X. Zhang, Q.J. Wang, 2D materials for photothermoelectric detectors: mechanisms, materials, and devices, Adv. Funct. Mater. 34 (2024) 2312872. https://doi.org/10.1002/adfm.202312872.
[8] W. Sha, Y. Wang, M. Xiao, Y. Fang, Z. Wang, S. Wang, W. Zeng, J. Zhao, L. Ruan, Conductive ionic thermoelectric hydrogel with negative seebeck coefficient, self-healing and highly sensitive to temperature for photothermoelectric conversion and non-contact sensing device, Chem. Eng. J. 501 (2024) 157823. https://doi.org/10.1016/j.cej.2024.157823.
[9] H. Liu, X. Jin, Q. Xu, Y. Jin, X. Zhang, S.-L. Lv, Integrated hydrogel-based photothermoelectric device for energy harvesting, ACS Appl. Mater. Interfaces (2025). https://doi.org/10.1021/acsami.5c07204.
[10] R. Wang, Y. Zhang, Z. Yu, C. Wang, F. Zhu, Y. Lai, J. Chen, W. Tian, Alginate-based functionalized, remote, light-responsive hydrogel transducer for synergistic mild photo thermoelectric stimulation for tumor therapy, Int. J. Biol. Macromol. 282 (2024) 136955. https://doi.org/10.1016/j.ijbiomac.2024.136955.
[11] M.E. Matter, C. Tagnon, E.E. Stache, Recent applications of photothermal conversion in organic synthesis, ACS Cent. Sci. 10 (2024) 1460, https://doi.org/10.1021/acscentsci.4c00545.
[12] B. Han, Y.L. Zhang, Q.D. Chen, H.B. Sun, Carbon-based photothermal actuators, Adv. Funct. Mater. 28 (2018) 1802235. https://doi.org/10.1002/adfm.201802235.
[13] Y. Ren, R. Lian, Z. Liu, G. Zhang, W. Wang, D. Ding, M. Tian, Q. Zhang, CNT/Polyimide fiber-based 3D photothermal aerogel for high-efficiency and long-lasting seawater desalination, Desalination 535 (2022) 115836. https://doi.org/10.1016/j.desal.2022.115836.
[14] W. Liu, X. Zhang, L. Zhou, L. Shang, Z. Su, Reduced graphene oxide (rGO) hybridized hydrogel as a near-infrared (NIR)/PH dual-responsive platform for combined chemo-photothermal therapy, J. Colloid Interface Sci. 536 (2019) 160. https://doi.org/10.1016/j.jcis.2018.10.050.
[15] Z. Han, D. Du, F. Zhang, CNTs composite aerogel incorporating phase-change microcapsules for solar-thermal conversion and energy storage, Carbon 237 (2025) 120125. https://doi.org/10.1016/j.carbon.2025.120125.
[16] L. Zeng, D. Deng, Y. Shen, X. Gu, Y. Yao, Highly efficient and stable solar-driven seawater desalination using composite photothermal structures with energy storage, Carbon 234 (2025) 119995. https://doi.org/10.1016/j.carbon.2025.119995.
[17] A. Ghosh, T. Sana Fathima, D. Ganguly, S. Ramaprabhu, Iron-oxide nanoparticle-decorated etched carbon nanotube catalysts for highly sensitive electrochemical detection of cholesterol and high-density lipoprotein (HDL), J. Electrochem. Soc. 172 (2025) 077511. https://doi.org/10.1007/s00604-024-06622-8.
[18] J. Shen, C. Yang, Y. Ma, M. Cao, Z. Gao, S. Wang, J. Li, S. Liu, Z. Chen, S. Li, Photo-thermo-electric hydrogel with interlocking photothermal layer and hydrogel for enhancement of thermopower generation, EcoMat 6 (2024) e12428, https://doi.org/10.1002/eom2.12428.
[19] C. Bai, X. Li, X. Cui, X. Yang, X. Zhang, K. Yang, T. Wang, H. Zhang, Transparent stretchable thermogalvanic PVA/Gelation hydrogel electrolyte for harnessing solar energy enabled by a binary solvent strategy, Nano Energy 100 (2022) 107449, https://doi.org/10.1016/j.nanoen.2022.107449.
[20] C. Norioka, Y. Inamoto, C. Hajime, A. Kawamura, T. Miyata, A universal method to easily design tough and stretchable hydrogels, NPG Asia Mater. 13 (2021) 34. https://doi.org/10.1038/s41427-021-00302-2.

[21] M.-H. Lin, S.-H. Hong, J.-F. Ding, C.-L. Liu, Organic porous materials and their nanohybrids for next-generation thermoelectric application, ACS Appl. Mater. Interfaces 16 (2024) 67116. https://doi.org/10.1021/acsami.4c12729.
[22] Y.-C. Hsiao, L.-C. Lee, Y.-T. Lin, S.-H. Hong, K.-C. Wang, S.-H. Tung, C.-L. Liu, Stretchable polyvinyl alcohol and sodium alginate double network ionic hydrogels for low-grade heat harvesting with ultrahigh thermopower, Mater. Today Energy 37 (2023) 101383. https://doi.org/10.1016/j.mtener.2023.101383.
[23] W. Shi, N. Song, Y. Huang, W. Wang, C. He, W. Zhao, C. Zhao, Enhanced thermal conductive and moisturizing hydrogels by constructing 3D networks of BN-OH and CNT-OH in alignment for burn therapy, Mater. Des. 233 (2023) 112239. https://doi.org/10.1016/j.matdes.2023.112239.
[24] H.S. Mansur, C.M. Sadahira, A.N. Souza, A.A.P. Mansur, FTIR spectroscopy characterization of poly (vinyl alcohol) hydrogel with different hydrolysis degree and chemically crosslinked with glutaraldehyde, Mater. Sci. Eng.: C 28 (2008) 539. https://doi.org/10.1016/j.msec.2007.10.088.
[25] R. Shanmugam, P. Dineshkumar, T. Sangeetha, P. Mounica, K. Ramya, A. Elangovan, G. Arivazhagan, Monomer, cyclic dimer of dimethyl sulfoxide, and dimethyl sulfoxide-water hydrogen bonded complexes: FTIR studies and quantum chemical calculations, J. Mol. Model. 31 (2025) 85. https://doi.org/10.1007/s00894-025-06300-3.
[26] Y.-S. Jun, X. Wu, D. Ghim, Q. Jiang, S. Cao, S. Singamaneni, Photothermal membrane water treatment for two worlds, Acc. Chem. Res. 52 (2019) 1215, https://doi.org/10.1021/acs.accounts.9b00012.
[27] W. Lei, Y. Liu, S. Khan, N. Suzuki, C. Terashima, A. Fujishima, M. Liu, Synergistically regulated surface structure and water transportation of sponge hydrogel evaporator for efficient water desalination, Desalination 533 (2022) 115780. https://doi.org/10.1016/j.desal.2022.115780.
[28] X. Zhou, F. Zhao, Y. Guo, Y. Zhang, G. Yu, A hydrogel-based antifouling solar evaporator for highly efficient water desalination, Energy Environ. Sci. 11 (2018) 1985. https://doi.org/10.1039/C8EE00567B.
[29] R.R. Anderson, H. Beck, U. Bruggemann, W. Farinelli, S.L. Jacques, J.A. Parrish, Pulsed photothermal radiometry in turbid media: internal reflection of backscattered radiation strongly influences optical dosimetry, Appl. Opt. 28 (1989) 2256. https://doi.org/10.1364/ao.28.002256.
[30] O. Tretinnikov, S. Zagorskaya, Determination of the degree of crystallinity of poly (vinyl alcohol) by FTIR spectroscopy, J. Appl. Spectrosc. 79 (2012) 521. https://doi.org/10.1007/s10812-012-9634-y.
[31] H. Cheng, Q. Le, Z. Liu, Q. Qian, Y. Zhao, J. Ouyang, Ionic thermoelectrics: principles, materials and applications, J. Mater. Chem. C 10 (2022) 433. https://doi.org/10.1039/D1TC05242J.
[32] D. Zhao, H. Wang, Z.U. Khan, J. Chen, R. Gabrielsson, M.P. Jonsson, M. Berggren, X. Crispin, Ionic thermoelectric supercapacitors, Energy Environ. Sci. 9 (2016) 1450. https://doi.org/10.1039/C6EE00121A.
[33] S.T. Kao, C.C. Hsu, S.H. Hong, U.S. Jeng, C.H. Wang, S.H. Tung, C.L. Liu, Host–guest complexation of α-Cyclodextrin and triiodide ions for enhanced performance of ionic thermoelectric capacitors, Adv. Energy Mater. 15 (2025) 2405502. https://doi.org/10.1002/aenm.202405502.
[34] Y.-S. Jheng, L.-C. Lee, S.-H. Hong, C.-C. Hsu, Q.-B. Zheng, C.-H. Wang, U.-S. Jeng, S.-H. Tung, C.-L. Liu, Sustainable and recyclable ionogels for ionic thermoelectric supercapacitor application, J. Mater. Chem. A 13 (2025) 10655. https://doi.org/10.1039/D5TA00734H.
[35] S. Zhou, X.L. Shi, L. Li, Q. Liu, B. Hu, W. Chen, C. Zhang, Q. Liu, Z.G. Chen, Advances and outlooks for carbon nanotube-based thermoelectric materials and devices, Adv. Mater. 37 (2025) 2500947. https://doi.org/10.1002/adma.202500947.
[36] Q. Sun, C. Du, G. Chen, Thermoelectric materials and devices: applications in enhancing building energy conversion and efficiency, Adv. Nanocompos. 2 (2025) 15. https://doi.org/10.1016/j.adna.2024.11.001.
[37] C. Zhang, X. Liu, S. Han, M. Wu, R. Xiao, S. Chen, G. Chen, High-performance n-type organic thermoelectric aerogels toward flexible energy harvesting and sensing devices, Adv. Electron. Mater. (2025) 2400824. https://doi.org/10.1002/aelm.202400824.
[38] Q. Le, H. Cheng, J. Ouyang, An ionic thermoelectric capacitor with continuous power generation for heat harvesting, Chem. Eng. J. 469 (2023) 143828. https://doi.org/10.1016/j.cej.2023.143828.
[39] Y.-H. Wang, C.-C. Hsu, S.-H. Hong, J.-F. Ding, U.-S. Jeng, D.-Y. Kang, S.-C. Luo, S.-H. Tung, C.-L. Liu, A dual-function poly(vinyl alcohol) hydrogel for solar water production and thermoelectric energy generation, ACS Sustainable Chem. Eng. 13 (2025) 4231. https://doi.org/10.1021/acssuschemeng.4c10855.
[40] Y.H. Pai, J. Tang, Y. Zhao, Z. Liang, Ionic organic thermoelectrics with impressively high thermopower for sensitive heat harvesting scenarios, Adv. Energy Mater. 13 (2023) 2202507. https://doi.org/10.1002/aenm.202202507.
[41] X. Lu, Z. Mo, Z. Liu, Y. Hu, C. Du, L. Liang, Z. Liu, G. Chen, Robust, efficient, and recoverable thermocells with zwitterion-boosted hydrogel electrolytes for energy-autonomous and wearable sensing, Angew. Chem. Int. Ed. (2024) e202405357. https://doi.org/10.1002/anie.202405357.
[42] X. Guan, H. Cheng, J. Ouyang, Significant enhancement in the seebeck coefficient and power factor of thermoelectric polymers by the soret effect of polyelectrolytes, J. Mater. Chem. A 6 (2018) 19347. https://doi.org/10.1039/C8TA08387H.
[43] C.Y. Lee, S.H. Hong, C.L. Liu, Recent progress in polymer gel-based ionic thermoelectric devices: materials, methods, and perspectives, Macromol. Rapid Commun. 46 (2025) 2400837. https://doi.org/10.1002/marc.202400837.
[44] X.-L. Shi, N.-H. Li, M. Li, Z.-G. Chen, Toward efficient thermoelectric materials and devices: advances, challenges, and opportunities, Chem. Rev. (2025). https://doi.org/10.1021/acs.chemrev.5c00060.
[45] S.-H. Hong, C.-C. Hsu, T.-H. Liu, T.-C. Lee, S.-H. Tung, H.-L. Chen, J. Yu, C.-L. Liu, Extremely large seebeck coefficient of gelatin methacryloyl (GelMA)-based thermogalvanic cells by the dual effect of ion-induced crystallization and nanochannel control, Mater. Today Energy 42 (2024) 101546. https://doi.org/10.1016/j.mtener.2024.101546.
[46] M. Mihajlovic, M. Mihajlovic, P.Y. Dankers, R. Masereeuw, R.P. Sijbesma, Carbon nanotube reinforced supramolecular hydrogels for bioapplications, Macromol. Biosci. 19 (2019) 1800173. https://doi.org/10.1002/mabi.201800173.
[47] N. Kamoshida, S. Kasahara, N. Ikemiya, N. Hoshi, M. Nakamura, Y. Einaga, In situ ATR-IR study of $Fe(CN)_6^{3-}/Fe(CN)_6^{4-}$ redox system on boron-doped diamond electrode, Diam. Relat. Mater. 93 (2019) 50. https://doi.org/10.1016/j.diamond.2019.01.021.
[48] K. Kim, S. Hwang, H. Lee, Unravelling ionic speciation and hydration structure of Fe (III/II) redox couples for thermoelectrochemical cells, Electrochim. Acta 335 (2020) 135651. https://doi.org/10.1016/j.electacta.2020.135651.
[49] G. Chen, Thermodynamics of hydrogels for applications in atmospheric water harvesting, evaporation, and desalination, Phys. Chem. Chem. Phys. 24 (2022) 12329. https://doi.org/10.1039/D2CP00356B.
[50] R.A. Huggins, Simple method to determine electronic and ionic components of the conductivity in mixed conductors a review, Ionics 8 (2002) 300. https://doi.org/10.1007/BF02376083.
[51] S. Wang, M. Yan, Y. Li, C. Vinado, J. Yang, Separating electronic and ionic conductivity in mix-conducting layered lithium transition-metal oxides, J. Power Sources 393 (2018) 75. https://doi.org/10.1016/j.jpowsour.2018.05.005.
[52] S.M. Khoshfetrat, In situ synthesis of nickel-substituted zeolitic metal-organic framework on Ti_3C_2 MXene for enhanced electrocatalytic sensing of L-tryptophan, J. Electroanal. Chem. 992 (2025) 119215. https://doi.org/10.1016/j.jelechem.2025.119215.
[53] S.M. Khoshfetrat, M. Motahari, S. Mirsian, 3D porous structure of ionic liquid-delaminated Ti_3C_2 MXene nanosheets for enhanced electrochemical sensing of tryptophan in real samples, Sci. Rep. 15 (2025) 6804. https://doi.org/10.1038/s41598-025-91773-8.
[54] B. Wang, S.M. Khoshfetrat, H. Mohamadimanesh, Peroxidase-like manganese oxide nanoflowers-delaminated Ti_3C_2 MXene for ultrasensitive dual-mode and real-time detection of H_2O_2 released from cancer cells, Microchem. J. 207 (2024) 111796. https://doi.org/10.1016/j.microc.2024.111796.
[55] S.M. Khoshfetrat, M. Moradi, H. Zhaleh, M. Hosseini, Multifunctional methyl orange-delaminated Ti_3C_2 MXene for non-enzymatic/metal-free electrochemical detection of hydrogen peroxide and hydrazine, Microchem. J. 205 (2024) 111382. https://doi.org/10.1016/j.microc.2024.111382.
[56] S.M. Khoshfetrat, S. Mamivand, G.B. Darband, Hollow-like three-dimensional structure of methyl orange-delaminated Ti_3C_2 MXene nanocomposite for high-performance electrochemical sensing of tryptophan, Microchim. Acta 191 (2024) 546. https://doi.org/10.1007/s00604-024-06622-8.
[57] L. Garrido, I. Aranaz, A. Gallardo, C. García, N. García, E. Benito, J. Guzmán, Ionic conductivity, diffusion coefficients, and degree of dissociation in lithium electrolytes, ionic liquids, and hydrogel polyelectrolytes, J. Phys. Chem. B 122 (2018) 8301. https://doi.org/10.1021/acs.jpcb.8b06424.
[58] Y. Lee, J.-H. So, H.-J. Koo, A transparent hydrogel-ionic conductor with high water retention and self-healing ability, Materials 17 (2024) 288. https://doi.org/10.3390/ma17020288.
[59] M. Zhang, Z. Che, J. Chen, H. Zhao, L. Yang, Z. Zhong, J. Lu, Experimental determination of thermal conductivity of water−agar gel at different concentrations and temperatures, J. Chem. Eng. Data 56 (2011) 859. https://doi.org/10.1021/je100570h.
[60] L.E. Ehrlich, J.S. Feig, S.N. Schiffres, J.A. Malen, Y. Rabin, Large thermal conductivity differences between the crystalline and vitrified states of DMSO with applications to cryopreservation, PLoS One 10 (2015) e0125862. https://doi.org/10.1371/journal.pone.0125862.
[61] O. Shih, K.-F. Liao, Y.-Q. Yeh, C.-J. Su, C.-A. Wang, J.-W. Chang, W.-R. Wu, C.-C. Liang, C.-Y. Lin, T.-H. Lee, Performance of the new biological small-and wide-angle X-ray scattering beamline 13A at the Taiwan photon source, Appl. Crystallogr. 55 (2022) 340. https://doi.org/10.1107/S1600576722001923.
[62] S. Park, B. Kim, C. Cho, E. Kim, Mesogenic polymer composites for temperature-programmable thermoelectric ionogels, J. Mater. Chem. A 10 (2022) 13958. https://doi.org/10.1039/D2TA03120E.
[63] Y.-T. Lin, C.-C. Hsu, S.-H. Hong, L.-C. Lee, U.S. Jeng, H.-L. Chen, S.-H. Tung, C.-L. Liu, Highly conductive triple network hydrogel thermoelectrochemical cells with low-grade heat harvesting, J. Power Sources 609 (2024) 234647. https://doi.org/10.1016/j.jpowsour.2024.234647.
[64] C.-Y. Lee, Y.-T. Lin, S.-H. Hong, C.-H. Wang, U.S. Jeng, S.-H. Tung, C.-L. Liu, Mixed ionic–electronic conducting hydrogels with carboxylated carbon nanotubes for high performance wearable thermoelectric harvesters, ACS Appl. Mater. Interfaces 15 (2023) 56072. https://doi.org/10.1021/acsami.3c09934.
[65] D. Gupta, M. Jassal, A.K. Agrawal, The electrospinning behavior of poly(vinyl alcohol) in DMSO–Water binary solvent mixtures, RSC Adv. 6 (2016) 102947. https://doi.org/10.1039/C6RA15017A.
[66] S. Otarbayeva, D. Berillo, Poly(vinyl alcohol) drug and PVA–Drug–Surfactant complex organogel with dimethyl sulfoxide as a drug delivery system, Gels 10 (2024) 753. https://doi.org/10.3390/gels10110753.
[67] H. Adelnia, R. Ensandoost, S.S. Moonshi, J.N. Gavgani, E.I. Vasafi, H.T. Ta, Freeze/Thawed polyvinyl alcohol hydrogels: present, past and future, Eur. Polym. J. 164 (2022) 110974. https://doi.org/10.1016/j.eurpolymj.2021.110974.
[68] N.M. Hapipi, S.A. Mazlan, U. Ubaidillah, S.A. Abdul Aziz, M.H. Ahmad Khairi, N. A. Nordin, N. Nazmi, Solvent dependence of the rheological properties in hydrogel

magnetorheological plastomer, Int. J. Mol. Sci. 21 (2020) 1793. https://doi.org/10.3390/ijms21051793.

[69] Q. Chen, B. Cheng, Z. Wang, X. Sun, Y. Liu, H. Sun, J. Li, L. Chen, X. Zhu, L. Huang, Rarely negative-thermovoltage cellulose ionogel with simultaneously boosted mechanical strength and ionic conductivity via ion-molecular engineering, J. Mater. Chem. A 11 (2023) 2145. https://doi.org/10.1039/D2TA09068F.

[70] M.M. Villar-Chavero, J.C. Domínguez, M.V. Alonso, M. Oliet, F. Rodriguez, Tuning the rheological properties of cellulosic ionogels reinforced with chitosan: the role of the deacetylation degree, Carbohydr. Polym. 207 (2019) 775. https://doi.org/10.1016/j.carbpol.2018.12.041.